doi.org/10.1002/chem.202004270
Check for updates
Chemistry Europe
European Chemical Societies Publishing

Positron Annihilation

Zinc Oxide Defect Microstructure and Surface Chemistry Derived from Oxidation of Metallic Zinc: Thin-Film Transistor and Sensor Behavior of ZnO Films and Rods

Rudolf C. Hoffmann,[a] Shawn Sanctis,[a] Maciej O. Liedke,[b] Maik Butterling,[b] Andreas Wagner,[b] Christian Njel,[c] and Jörg J. Schneider*[a]

Abstract: Zinc oxide thin films are fabricated by controlled oxidation of sputtered zinc metal films on a hotplate in air at temperatures between 250 and 450 °C. The nanocrystalline films possess high relative densities and show preferential growth in (100) orientation. Integration in thin-film transistors reveals moderate charge carrier mobilities as high as 0.2 $cm^2V^{-1}s^{-1}$. The semiconducting properties depend on the calcination temperature, whereby the best performance is achieved at 450 °C. The defect structure of the thin ZnO film can be tracked by Doppler-broadening positron annihilation spectroscopy as well as positron lifetime studies. Comparably long positron lifetimes suggest interaction of zinc vacancies (V_{Zn}) with one or more oxygen vacancies (V_O) in larger structural entities. Such V_O-V_{Zn} defect clusters act as shallow acceptors, and thus, reduce the overall electron conductivity of the film. The concentration of these defect clusters decreases at higher calcination temperatures as indicated by changes in the S and W parameters. Such zinc oxide films obtained by conversion of metallic zinc can also be used as seed layers for solution deposition of zinc oxide nanowires employing a mild microwave-assisted process. The functionality of the obtained nanowire arrays is tested in a UV sensor device. The best results with respect to sensor sensitivity are achieved with thinner seed layers for device construction.

Introduction

Zinc oxide is an important semiconducting and piezoelectric material, which has gained considerable attention over the last decade as a promising candidate for various microelectronic, optoelectronic, and sensing applications.[1–3] Thus, impressive charge carrier mobilities above 50 $cm^2V^{-1}s^{-1}$ have been observed in thin-film transistors (TFTs) obtained from sputter deposition of ZnO.[4,5] That said, zinc oxide layers fabricated by means of solution deposition, which is hailed as a cost-efficient approach enabling coating under temperatures suitable for sensitive substrates, frequently exhibit rather poor performances.[6] In part, this might be caused by the architecture of the TFT devices under study. However, the question remains how a distinct deposition process might influence the observed electronic properties.[7] The observed lack of performance in such solution-processed ZnO semiconductors is commonly attributed to poor interface quality and high porosity, as well as contamination by organic residues.[8] Frequently, annealing improves the performance of a TFT, which affects both the microstructure of the film and its defect chemistry. Sintering causing grain growth and lower porosity is, however, rarely observed in the temperature range (< 500 °C) in question.[9] On the other hand, thermal treatments have a drastic influence on the adsorbates[10] on the surface of the thin film, as well as on the nature of point defects[11] within the metal oxide lattice. Such effects can be monitored using spectroscopic techniques such as electron paramagnetic resonance (EPR), photoluminescence (PL) spectroscopy, or X-ray photoelectron spectroscopy (XPS).[12] The attribution of distinct signals to the various types of possible point defects is, however, a nontrivial task, and remains cumbersome.

[a] Dr. R. C. Hoffmann, Dr. S. Sanctis, Prof. Dr. J. J. Schneider
Eduard-Zintl-Institute for Inorganic and Physical Chemistry
Technical University Darmstadt
Alarich-Weiss-Straße 12, 64287 Darmstadt (Germany)
E-mail: joerg.schneider@ac.chemie.tu-darmstadt.de

[b] Dr. M. O. Liedke, Dr. M. Butterling, Dr. A. Wagner
Institute of Radiation Physics
Helmholtz-Zentrum Dresden-Rossendorf
Bautzner Landstraße 400, 01328 Dresden (Germany)

[c] Dr. C. Njel
Institute for Applied Materials—Energy Storage
Karlsruhe Institute of Technology (KIT)
Hermann-von-Helmholtz-Platz 1
76344 Eggenstein- Leopoldshafen (Germany)

Supporting information and the ORCID identification number(s) for the author(s) of this article can be found under: https://doi.org/10.1002/chem.202004270.

© 2020 The Authors. Chemistry - A European Journal published by Wiley-VCH GmbH. This is an open access article under the terms of the Creative Commons Attribution Non-Commercial NoDerivs License, which permits use and distribution in any medium, provided the original work is properly cited, the use is non-commercial and no modifications or adaptations are made.

© 2020 The Authors. Chemistry - A European Journal published by Wiley-VCH GmbH

All as-grown ZnO samples are unintentionally n-type, the cause of which is still under debate.[13] In the past, many research groups have claimed that this inherent conductivity is caused by oxygen vacancies (V_O) or zinc interstitials (Zn_i).[14] This assignment is based on experiments showing the dependence of the conductivity as a function of oxygen partial pressure, but in the end remains ambiguous.[15] Other possible intrinsic defects such as zinc anti-sites, oxygen interstitials, or oxygen anti-sites even have higher formation energies, and are therefore highly unlikely.[11] In contrast, several recent studies and calculations hint at the relevance of multiple defects, in which clustering and/or pairing occurs and leads to increased stability.[16] It has been shown that V_{Zn} and V_O appear simultaneously and remain as nearest neighbors, either as divacancies V_{Zn}-V_O or as vacancy clusters V_{Zn}-$(V_O)_n$.[17] Recently, density functional calculations also predicted strong interactions between V_O and Zn_i sites.[18]

In-depth studies attempting to correlate the electronic properties of TFTs with the corresponding thin-film microstructure and point defects are still scarce.[2]

The present work will address the latter point by employing positron annihilation spectroscopy, that is, lifetime spectra (PALS), 3γ/2γ spectroscopy, as well as coincidence Doppler broadening (DB-PAS).[19,20] This approach is unique, and will help to understand the semiconducting behavior of the films. In searching for a suitable synthetic approach for a model system, we found that the synthesis of zinc oxide nanoparticles or thin films by oxidation of zinc metal has rarely been studied so far.[21,22] This comes as a surprise, as it should be a convenient approach and would avoid especially organic contamination, which is often introduced if using solution-based approaches. Furthermore, subsequent ZnO nanowire array deposition and its integration in a UV sensor is studied.

Results and Discussion

Synthesis and microstructure of ZnO thin films

Films of metallic zinc of various thicknesses (10–75 nm) are deposited on quartz or silicon/silicon oxide (230 nm) substrates using RF magnetron sputtering. Thinner films of the metal (below 50 nm) exhibit a dark color, but turn to a slightly lighter appearance upon standing in air at room temperature. Only thicker films (≈75 nm) have a persistent greyish color. All samples, however, are transparent after annealing at temperatures between 150 and 450 °C on a hot plate. This procedure keeps the contact to the initial heating stage to a minimum and avoids contamination coming from inside the furnace, which could be detrimental for any electronic or optical applications (noted that furnaces are often used for preparing such thin films).

SEM images of the obtained films reveal a granular structure, and differences in the morphology before and after annealing are almost undiscernible (Figure 1 a and Figure S1, Supporting Information). The UV/Vis spectra (Figure 1 b) show the expected absorption for ZnO in the range 360–390 nm depending on

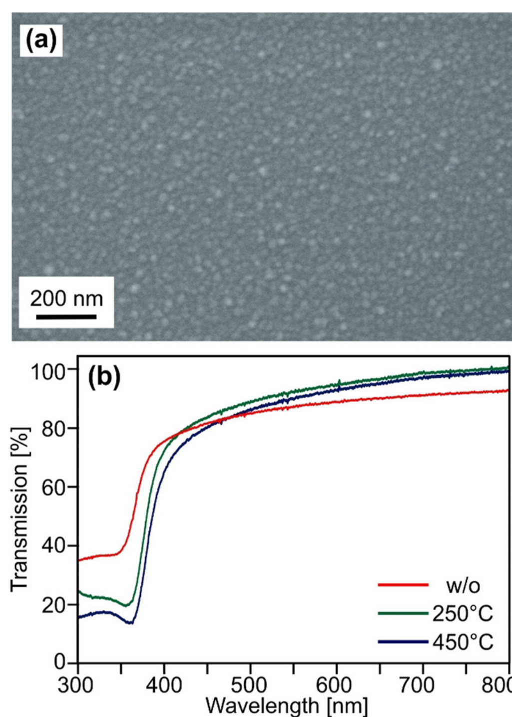

Figure 1. a) SEM image depicting ZnO film obtained from sputter deposition of 75 nm zinc and oxidation in air at 450 °C. b) UV/Vis spectra of films obtained from sputter deposition of 50 nm zinc and oxidation in air at various temperatures.

the calcination temperature, and the bathochromic shift indicates the expected crystallite growth.

The surface composition was analyzed by XPS for as-prepared films from sputter deposition as well as for samples also annealed at temperatures of 250 and 450 °C. Spectra in the energy range of Zn 2p, O 1s, and C 1s signals were recorded (Figure S2, Supporting Information). The Zn 2p peak can be assigned to one contribution at approximately 1021.6 eV, which is in accordance with the presence of ZnO. No indication of metallic Zn is evident.[23] The O 1s spectra are deconvoluted with two components, arising at about 530 and 532 eV, reflecting contributions from oxidic oxygen as well as OH surface hydroxylation.[24] A reduction in the contribution from the M–OH peak and the corresponding increase in the M–O peak is found upon comparing different annealing temperatures (250 and 450 °C). XPS depth profiles indicate that hydroxylation does not occur exclusively at the surface, but is an inherent part of the ZnO films. The C 1s region comprises components that indicate the presence of C–O or C=O species. The relative amount is highest in the as-deposited specimens that were not subjected to further annealing. The binding energies of all peaks in the C 1s region, however, are well below the value expected for carbonate ions (which are conversely also not visible in the O 1s region). The corrosion of zinc metal as well zinc alloys has been studied in depth by means of XPS.[25,26] The formation of hydrozincite or other basic zinc salts is not observed in dry air or in the absence of further ions such as halides.[25,27] On the other hand, distinguishing and identifying the different types of carbon species that coexist in a particular corrosion

© 2020 The Authors. Chemistry - A European Journal published by Wiley-VCH GmbH
These are not the final page numbers!

layer on metallic zinc can be cumbersome, especially if the position of adventitious carbon is not carefully developed.[28]

Similarly, annealed films were investigated by means of X-ray diffraction (XRD) (Figure 2). The observed patterns comprise only peaks of wurtzite (JCPDS card #36–1451), and no further contributions were visible. A preferential growth in the (100) direction is observed. This type of texture formation in ZnO films obtained from oxidation of metallic zinc is not completely unprecedented, but such reports are rare.[29,30]

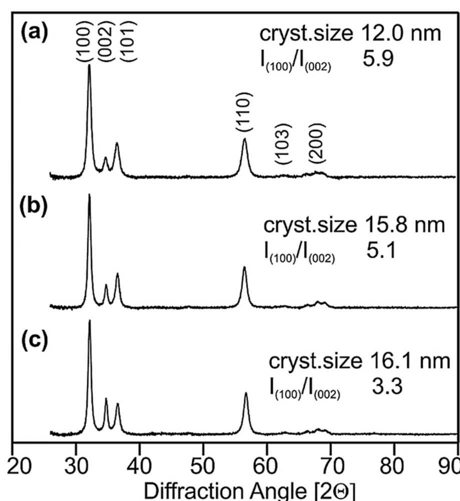

Figure 2. X-ray diffractograms of ZnO layers on quartz after annealing at different temperatures: a) 250 °C, b) 350 °C, and c) 450 °C. Miller indices correspond solely to wurtzite (JCPDS card #36–1451).

Mostly, preferential growth in the (002) direction[31,32] or random orientation of grains[33,34] have been reported. These differences are presumably attributable to the employed reaction conditions, as the texture can be controlled by the residual oxygen in the deposition process of the zinc metal and the presence of moisture during the oxidation in air. This is in accordance with suggestions that polar surfaces in ZnO are stabilized by point defects or surface adsorbates.[35,36] The XRD patterns (Figure 2) also reveal that the relative intensities of the signals corresponding to the low-index planes changed. Calcination at higher temperatures leads to a significant increase in the (002) peak with respect to the (100) and (101) peaks. This may be caused by the grain growth that occurs during annealing after the oxidation of the zinc metal. Earlier studies on the evolution of the microstructure of nanocrystalline ZnO during sintering have reported faster growth of grains in the direction of the *c* axis.[37–39]

ZnO coatings on silicon/silicon dioxide substrates show bright interference colors, which do not change even after sintering. This already indicates that the ZnO films possess a rather high relative density. In the following, the compaction behavior of the ZnO films was studied by means of ellipsometry (Figure 3). Indeed, the observed changes are rather low (below ≈10% even after calcination at 450 °C).

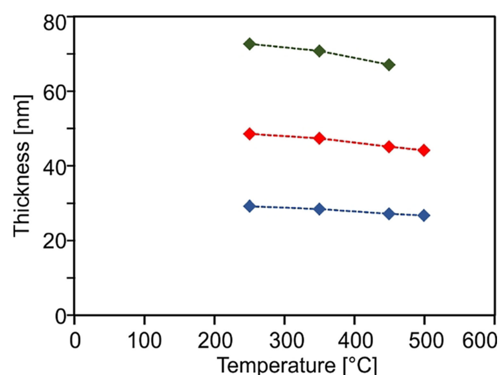

Figure 3. Thickness of ZnO layers depending on calcination temperature, as determined by ellipsometry. Three sets of samples differing in the initial thickness of the zinc metal (green 75 nm; red 50 nm; blue 30 nm) are compared.

Fabrication of a thin-film transistor (TFT) device

For the study of the electronic properties of the ZnO films, thin-film transistors were fabricated, employing the ZnO films as a semiconducting layer. The device setup is a bottom gate/bottom electrode arrangement (Figure S3, Supporting Information) with highly doped silicon as gate and support, silicon dioxide acting as dielectric, and gold electrodes with an interdigital geometry as source and drain electrodes. The ZnO film was calcined at temperatures of 250, 350, and 450 °C, respectively, after sputter deposition. This additional annealing step is necessary to achieve a reasonable performance.

A summary of the performance parameters (charge carrier mobility μ_{SAT}, on/off ratio $I_{on/off}$, and threshold voltage V_{th}) determined from the measurements is depicted in Figure 4a. Higher calcination temperatures lead to an increase in the charge carrier mobility as well as the on/off ratio, whereas the threshold voltage decreased. Thus, the best performance is obtained at a calcination temperature of 450 °C, at which no obvious hysteresis is observed (Figure 4b,c). To the best of our knowledge, only one comparable study (Yoo et al.) exists with a bottom gate/top electrode architecture employing a ZnO thin film as semiconductor.[40] Films are grown employing reactive sputtering and substrate temperatures of 450 °C. Whereas as-deposited films are conductive and unsuitable as semiconductors, reduction in a hydrogen atmosphere leads to devices with μ_{SAT} = 6.5 $cm^2V^{-1}s^{-1}$, $I_{on/off}=5\times10^6$, and $V_{th}=-5$ V (meaning the TFT was already "on" at 0 V). Such high charge carrier mobilities can otherwise only be achieved using RF-magnetron sputtering of zinc oxide or using atomic layer deposition (ALD).[41,42] As Yoo et al. do not provide any meaningful characterization of the microstructure or the defect chemistry, a clear explanation for the difference is not easy. In fact, there are not many techniques that provide extensive insight into a semiconductor thin film on a near-atomic level. That said, a notable example of a powerful method that can provide such essential information, being able to correlate defect structure with charge carrier behavior, is positron annihilation spectroscopy.[19,20]

© 2020 The Authors. Chemistry - A European Journal published by Wiley-VCH GmbH

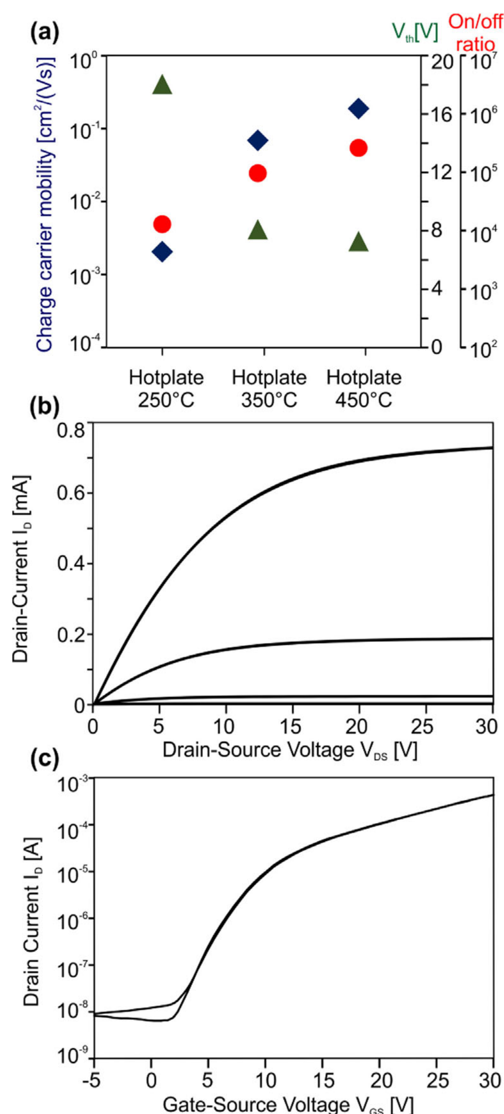

Figure 4. a) Performance parameters of FETs obtained from oxidation of zinc metal films (30 nm) and annealing at various temperatures. Output and transfer characteristics refer to the sample with a calcination temperature of 450 °C. b) Output characteristics obtained from variation of the drain-source voltage from 0–30 V for gate-source voltages from 0–30 V in 5 V steps. Data were acquired for increasing as well as decreasing drain-source voltages. c) Transfer characteristics for constant drain-source voltage of 30 V (μ_{SAT} = 0.20 cm^{2}V^{-1}s^{-1}, V_{th} = +7.3 V, $I_{on/off}$ ≈ 225,000).

DB-PAS and PALS measurements of ZnO films

In an attempt to correlate the semiconducting properties to the intrinsic microstructure of the ZnO thin films, we performed Doppler broadening investigations (DB-PAS) as well as lifetime measurements (PALS). Samples were prepared by sputter deposition of zinc metal (75 nm) on silicon/silicon oxide (230 nm) substrates and subsequent annealing (corresponding to Figures 1 a and 3).

The line shape of the γ-radiation peak resulting from the annihilation process in DB-PAS measurements is influenced by the momentum of the involved electrons. This allows differentiation between contributions of valence electrons or open-volume defects (S parameter) and core electrons (W parameter).[19] The course of the S and W parameters for various ZnO films on silicon/silicon oxide as a function of the implantation depth are presented in Figure 5 a,b. The implantation depth z is calculated as $z = AE^r/\eta$, in which A and r are empirical constants and η is the density of the material.[43]

All samples exhibit a comparable curve progression, whereby the courses of the S and W parameters show a minimum or a maximum, respectively. The positions of the extrema do not shift with respect to the implantation energy, indicating a comparable film thickness of the ZnO layer, which is in agreement with the ellipsometry data. At higher annealing temperatures, a decrease in the S parameter and a concomitant increase in the W parameter is observed. This behavior reflects earlier in-

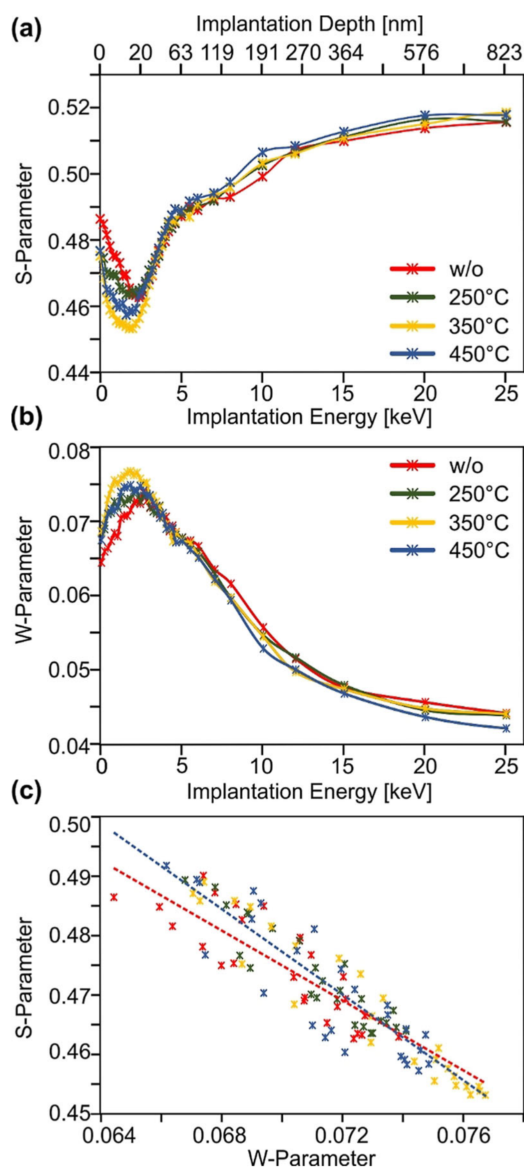

Figure 5. a) S and b) W parameters as function of implantation energy as well as corresponding calculated values for implantation depth in ZnO. Comparison of samples obtained under different processing conditions. c) S parameter as function of corresponding W parameters. Linear correlation functions are shown for the as-deposited and the annealed samples including separate correlation functions for the two data sets (dashed red for as-deposited samples and dashed blue for annealed samples).

© 2020 The Authors. Chemistry - A European Journal published by Wiley-VCH GmbH

vestigations on a series of doped and undoped ZnO films with different charge carrier mobilities by means of DB-PAS.[44,45] It is suggested that the observed changes are not in accordance with the presence of isolated Zn or O vacancies, but are caused by larger entities in which one or more oxygen vacancies can cluster around cation vacancies, that is, V_{Zn}-$(V_O)_n$.[19,46]

Among various native point defects in ZnO oxygen vacancies (V_O), zinc interstitials (Zn_i) are considered as possible donors, whereas zinc vacancies (V_{Zn}) and oxygen interstitials (O_i) may act as acceptors.[13] The O vacancy has a low formation energy, but is, however, a very deep donor, which makes it an unlikely candidate responsible for the n-type conductivity.[18] In contrast, recent theoretical calculations hint at the formation of defect complexes, in which one or more oxygen vacancies cluster around cation vacancies.[19] These defect complexes enjoy increased stability owing to coulombic attractions. Further, they act as shallow acceptors, and thus, suppress electron conductivity.[19,46] Apart from spectroscopic evidence, advanced transmission electron microscopic studies are currently emerging, which are able to prove the existence of zinc vacancies (V_{Zn}) directly.[47] Once trapped at such defect clusters sites, the positron is more in contact with low-momentum valence electrons than it is in the delocalized bulk state.[44,45]

A juxtaposition of S and W values from identical implantation energies (below 5.5 keV and thus below 75 nm implantation depth to ensure that only contributions of ZnO are taken into account) reveals a linear relation, and hints at one dominating type of defect in all annealed samples (Figure 5 c). However, the as-deposited sample differs drastically from its annealed counterparts. Thus, the S- and W-parameter spectra can clearly explain the observed TFT behavior (Figure 4).[48]

In another series of experiments, positron annihilation lifetime spectra (PALS) were recorded (Figure S4, Supporting Information). The curve fitting of these PALS spectra was performed with five lifetime components (Figure 6).

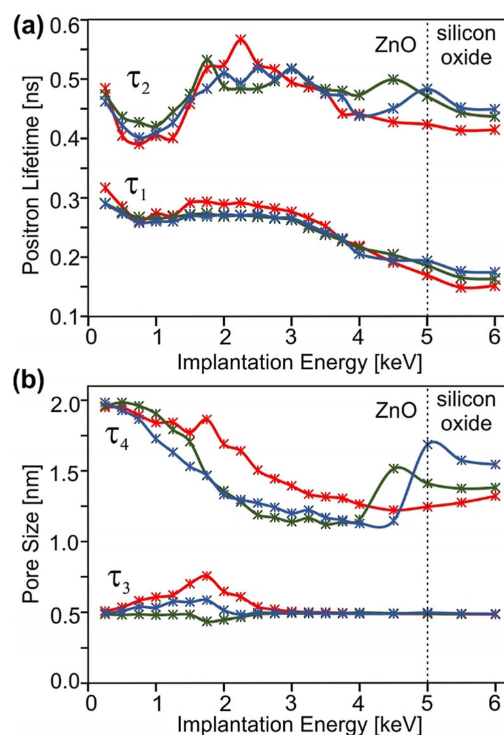

Figure 6. Depth profile derived from the curve fitting of the PALS spectra of ZnO film on silicon/silicon oxide substrates obtained at different temperatures (250 °C red, 350 °C green, and 450 °C blue). a) Values of the lifetime components τ_1 and τ_2 as a function of implantation energy. b) Pore diameters calculated from the lifetime components τ_3 and τ_4. The first and second lifetime components (τ_1 and τ_2) are caused by saturated positron trapping in large vacancy complexes (such as the abovementioned V_{Zn}-$(V_O)_n$) and voids in the ZnO film. The third and fourth contributions (τ_3 and τ_4) are attributed to the pores, and the fifth component evidences a small amount of *ortho*-positronium diffusing through the interparticle spaces into vacuum.

Despite the high ability of PALS to probe the characteristics of defects, a precise attribution and identification is not straightforward. Normally, the spectra of II–VI semiconductor compounds are caused by more than one type of defect or void, and are thus the superposition of several components with different lifetimes. Shorter lifetimes are attributed to intrinsic and extrinsic defects (such as vacancies or interstitials) within the bulk, as well as defects at interfaces and grain boundaries.[49]

In accordance with the abovementioned DB-PAS spectra, no drastic change in the contributions from the individual components for τ_1 and τ_2 was observed (Figure 6). Therefore, the dominating type of defect in all samples is the same, whereas its concentration might vary. As mentioned above, however, the identification and attribution of the observed lifetime components to intrinsic or extrinsic types of defects is not straightforward. On the basis of theoretical calculations, it can be said that the observed lifetimes are much too high for simple oxygen or zinc vacancies. Strong surface adsorbates are known to have a drastic influence on positron lifetimes, and would thus affect the values of τ_1 and τ_2.[50] As no major carbonaceous adsorbate layer is present at the surface after calcination at higher temperatures, such an effect can be excluded. Again, this confirms the overall picture of larger defect clusters extending over several sites within the zinc oxide lattice, rather than isolated point defects (see Figure 7).

The contributions of τ_3 and τ_4 could provide some insight into the micro- (≈0.5 nm) and mesoporosity (≈1–2 nm) of the ZnO films. A decrease in the pore size with higher annealing temperatures is observed. Interestingly, the size of the mesopores varies to a significantly larger extent than that of the micropores. Moreover, larger mesopores can be found at the film surface rather than at the zinc oxide/silicon oxide interface. The relative amount of τ_3 and τ_4 to the overall positron lifetime is below 5 %, and suggests a rather low porosity. This could be confirmed by the 3γ/2γ plot (Figure S5, Supporting Information). The 3γ/2γ ratio depends on the void size, whereby larger voids correlate with higher lifetimes and a higher 3γ/2γ value.

It should be taken into account that positron annihilation provides reliable information only up to a pore size of several nanometers. Thus, significantly larger inner pores would not be considered. The combined findings of the performed set of positron annihilation studies allow the development of a schematic defect picture of the ZnO thin films studied so far (Figure 7).

© 2020 The Authors. Chemistry - A European Journal published by Wiley-VCH GmbH

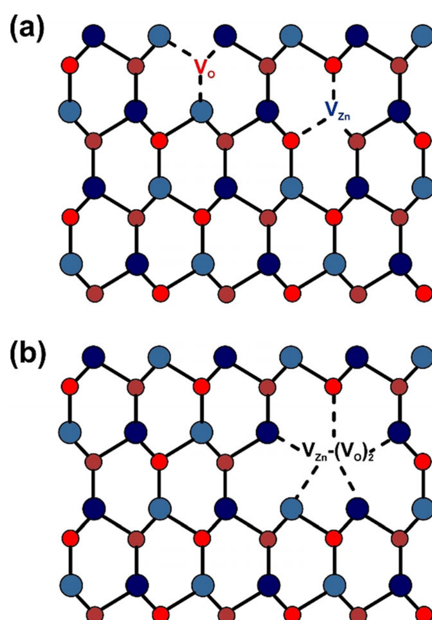

Figure 7. Model describing defect structure in wurtzite-type ZnO obtained from controlled thermal annealing of sputtered metallic films. a) Isolated oxygen and zinc vacancies. b) V_{Zn}-$(V_O)_2$ vacancy clusters.

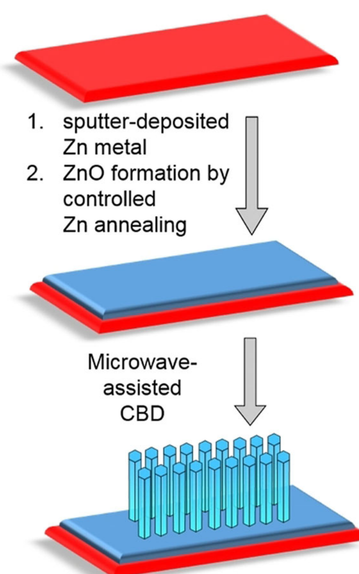

Figure 8. Illustration of seed layer fabrication and nanowire array deposition employing microwave-assisted processing. (Red: substrate, blue ZnO seed layer film).

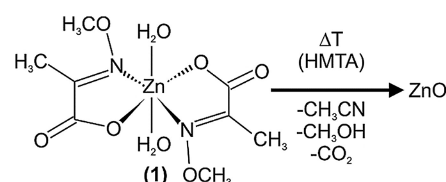

Scheme 1. Simplified presentation of the base-catalyzed decomposition of diaqua-bis[2-(methoxyimino) propanoato] zinc (**1**) into zinc oxide (wurtzite). The transformation into ZnO is characterized by expulsion of defined molecular products originating from the controlled degradation of the ligand framework.[57]

ZnO nanowire growth from seeded ZnO thin films

After the successful synthesis of the nanocrystalline ZnO layers, the suitability as a seed layer for the deposition of nanowire arrays was investigated. The established procedure makes use of chemical bath deposition (CBD) using zinc acetate and hexamethylene tetraamine (HMTA) for the nanowire growth.[51] Although this process is widely used, it has several drawbacks. The deposition of the nanowires takes a very long time (several hours) and uniform coating of larger areas (several square centimeters) is often problematic.[52] Therefore, to keep reaction times tolerably low, rather high concentrations have to be chosen. However, apart from the nanowire growth achieved on the seed layer, homogenous nucleation also occurs within the solution, which may in turn form deposits by sedimentation (Figure S6 a, Supporting Information).[53,54]

Improvements must therefore address these crucial points of the initial fabrication procedure. First, the time required for the deposition can be reduced drastically by performing the reaction under mild microwave heating (Figure 8).[55,56] Furthermore, alternative precursors should be considered. A zinc oximato complex $Zn(C_4H_6NO_3)_2(H_2O)_2$ (**1**) and HMTA have recently been employed as educts in the microwave-assisted mineralization solution (Scheme 1).[57] The oximato ligands are completely dismantled under basic conditions, which prohibits the formation of basic zinc salts as side products (Figure S6 b).

In the current work, the zinc oximato compound (**1**) and HMTA are employed with a concentration of 10 mM each, that is, a 1:1 molar ratio. Our reaction conditions hint toward the formation of an intermediate oxidic layer, which is formed on the bare zinc metal.[58] We found that growth occurred on sputtered metallic zinc layers even without additional calcination or annealing at lower temperatures. However, the best results with respect to uniformity of surface coverage and length of the resulting zinc oxide wires were obtained with metallic Zn films as seed layers, which were subsequently annealed at 450 °C prior to zinc oxide nanowire deposition (Figure S7, Supporting Information).[52,53] The thickness of the metallic zinc seed layer had an impact on the morphology of the resulting ZnO nanowires obtained by the microwave CBD process (Figure 9). It should be mentioned that no deposition of ZnO wires occurred at all without any prior seed layer deposition. Evidently, thicker seed layers obtained from 5, 20, and 40 nm zinc films led to higher diameters of ZnO wires of 45, 57, and 86 nm, respectively. The aspect ratio of the obtained ZnO nanowires was quite low, as the lengths did not exceed 220 nm.

The nanowire coatings were characterized by means of XRD (Figure 10). The contributions of the nanocrystalline seed layers to the diffractograms should be negligible owing to the comparably small layer thickness and the smaller crystallite size. In the diffractograms, only reflections related to wurtzite are visible. The ratios $I(100)/I(002)$ and $I(101)/I(002)$ change according to the seed layer thickness. In all cases the (002) peak

© 2020 The Authors. Chemistry - A European Journal published by Wiley-VCH GmbH

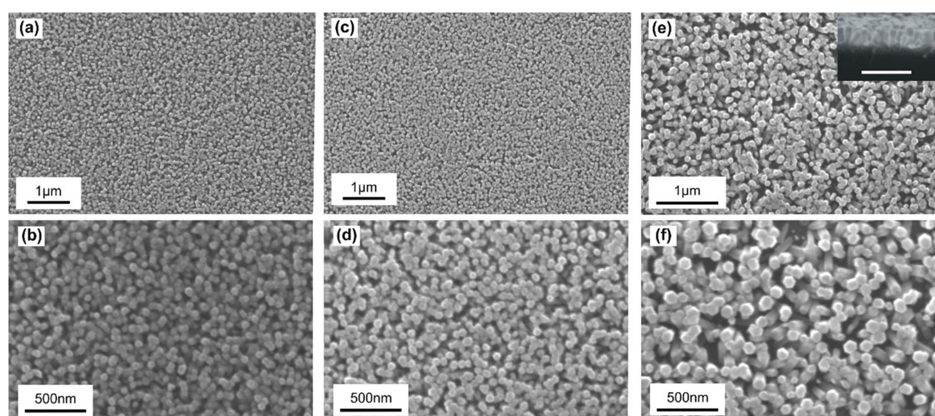

Figure 9. SEM images of ZnO nanowires deposited on metallic Zn seed layers obtained by sputtering zinc metal of different thickness and annealing at 450 °C: a,b) 5 nm, c,d) 20 nm, and e,f) 40 nm. The inset at the top in (e) depicts a cross-section of the particular sample (scale bar represents 500 nm).

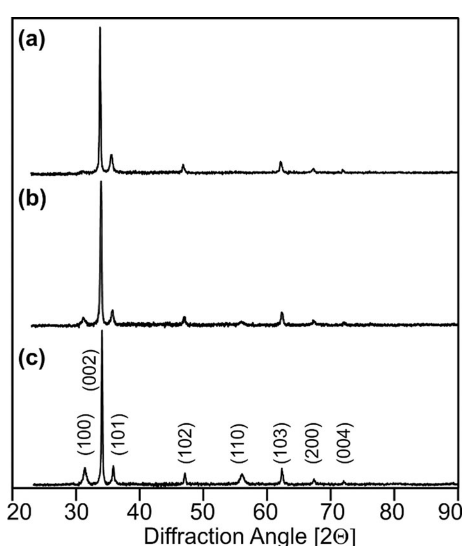

Figure 10. X-ray diffractograms of ZnO nanowires on quartz grown on seed layers obtained by sputtering zinc metal of different thickness and annealing at 450 °C: a) 5 nm, b) 20 nm, and c) 40 nm. Miller indices correspond to wurtzite (JCPDS card #36-1451).

has the highest intensity. However, with higher seed layer thicknesses, the relative intensity of (100) and (101) signals increases (Table S1, Supporting Information). Thus, interestingly, no growth of the CBD deposits occurs in the (100) direction. This finding is in accordance with earlier investigations dealing with the influence of the crystallographic orientation of the seed layer on the inclination of the nanowires grown thereon.[29,59,60] Epitaxial growth on nonpolar surfaces is well known for substrates with microcrystalline grains and well-defined textures.[29,60] The situation is different, however, on poorly textured, nanocrystalline seed layers with a range of nonpolar, semipolar, or polar crystal faces.[59] In these cases, the differences in the chemical nature of the various surfaces, for example, surface charge, oxygen dangling bond density, or degree of hydroxylation, play a significant role. These competitive effects typically favor preferential growth in the direction of the polar *c* axis. If the vertical alignment is not optimal, a number of different degrees of inclination might be observed. More detailed investigations would therefore involve the recording of pole figures, which is beyond the scope of the present study.

UV sensor derived from 1D arranged ZnO nanowires

The photoresponse of the prepared ZnO nanowire arrays (which necessarily includes a contribution from the underlying seed layer) is recorded as the current density under UV on/off conditions. Upon exposure of the ZnO to near-UV wavelengths, the photons create electron–hole pairs in the ZnO material. The holes migrate to the surface and recombine with oxygen ions, and the conductivity of the wire is increased by photoexcited electrons.[1,3] Thus, an interdigital arrangement of the electrodes is a well-proven low-footprint design for this purpose, which combines high electrode length with the demand for small area, and is therefore favorable for further integration and miniaturization.[61,62] For this work, the electrodes on the TFTs and the underlying isolation silicon oxide layer are employed as substrate (Figure 11). Although this device setup based on the TFT design would, in principle, even allow measurements with gate-voltage bias, this possibility is not used in the current work.[63,64]

The device was tested under UV light illumination (365 nm), with the light intensity (6 W) and distance of the UV lamp from the device (5 cm) kept constant. The influence of the seed layer thickness on the photoresponse was studied systematically (Figure 12). In a control experiment, layers obtained from the oxidation of zinc metal were measured without additional nanowires (Figure 12a).

Thicker zinc oxide films lead to slightly higher photocurrent densities, but do not change the overall activity pattern. The ZnO layers alone, however, exhibit a significantly lower photoresponse compared with the final sensor specimens with additional nanowire arrays (Figure 12b,c). The employed illumination times reveal the device limitations. The oxygen desorption is not reversible under ambient conditions and the current decreases with renewed illumination within a cycle. This is the case for all the investigated samples. The resulting morphologies of the nanowires grown on the seed layers vary so much

© 2020 The Authors. Chemistry - A European Journal published by Wiley-VCH GmbH

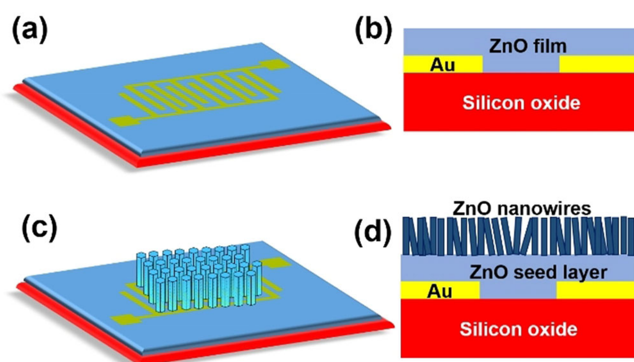

Figure 11. Schematic presentation of the two UV sensor designs employed in this work. a) Top view and b) cross-section of ZnO film obtained by sputtering on an interdigital gold structure. The interdigitated electrode structure is underneath the ZnO seed layer film and shown visible for clarity. Electrical contact of the gold electrode pads is achieved by penetrating needle probes punched into the ZnO seed layer. c) Top view and d) cross-section of ZnO nanowire arrays on ZnO seed layer integrated in electrode architecture.

that the resulting response/decay patterns exhibit stark differences.

Relaxation to zero current occurs only with nanowires on sufficiently thin seed layers (Figure 12b). Nanowire arrays deposited on thicker layers lead to a constant increase in the photocurrent (Figure 12c). Also, after stopping an illumination sequence within a cycle, no relaxation is observed. Presumably, resident charge carriers are created within the surface of the wires.[65,66] This effect exceeds the opposing effect of oxygen desorption. Thus, it can be shown that a UV sensor is obtained. Further improvement could involve nanowires with a higher aspect ratio (so-called "ultralong" wires).[61,62]

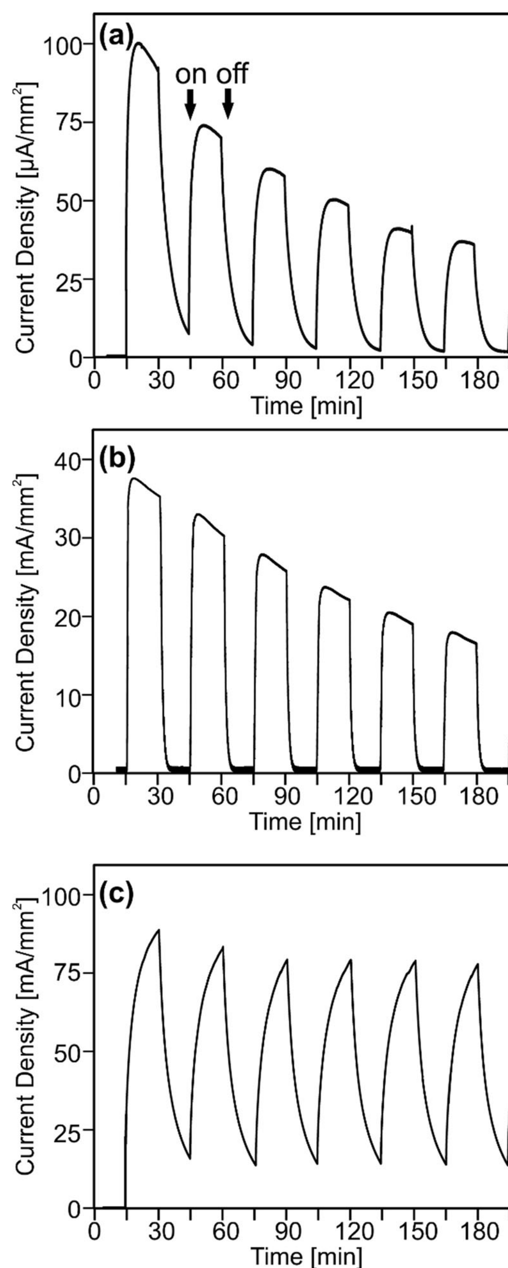

Figure 12. Photocurrent density as a function of time for a) substrate with seed layer (≈30 nm) only, b) with additional nanowire coating, and c) substrate with thicker seed layer (≈50 nm) and nanowire coating. The peaks correspond to illumination with UV light (365 nm) in intervals of 15 min.

The zinc oxide films can also be used as seed layers for the deposition of zinc nanowire arrays by microwave-assisted CBD. In this way, an active component for UV photodetection can be created. The change in resistivity caused by irradiation depends heavily on the thickness of the seed layer. First, this parameter affects the morphology of the resulting ZnO nanowires. Secondly, the contribution of the seed layer to the resulting conductivity cannot be neglected. We find that a thicker layer (from oxidation of 50 nm zinc metal) and the nanowire arrays grown upon them result in a constantly increasing photoresponse during irradiation, without reaching a constant current. In contrast, a thinner layer (from oxidation of 30 nm zinc

Conclusions

Zinc oxide layers with good semiconducting properties can be obtained conveniently through oxidation at temperatures between 250 and 450 °C from sputter-deposited thin films of zinc metal. The observed charge carrier mobilities as well as the $I_{on/off}$ ratios increase with higher processing temperatures, whereas the corresponding threshold voltages are reduced. Thus, the best results are observed at 450 °C with $\mu_{SAT}=0.20\ cm^2V^{-1}s^{-1}$, $V_{th}=+7.3$ V, and $I_{on/off}\approx 225{,}000$. The performance certainly benefits from an improved microstructure after annealing. Thus, at higher temperatures, densification occurs and the average crystallize size increase from 12.0 nm at 250 °C to 16.1 nm at 450 °C. Moreover, DB-PAS and PALS techniques can elaborate differences in the defect structures of the individual samples, and were employed successfully in this work. Both techniques provide proof of the existence and dominating influence of larger defect clusters, that is, larger entities in which one or more oxygen vacancies are discretely attached to cation vacancies. As these vacancy clusters $[V_{Zn}\text{-}(V_O)_n]$ are acceptor dopants, this type of point defect causes holes in the valence band of ZnO, and thus, leads to a significant drop in the electronic carriers, as observed experimentally.

© 2020 The Authors. Chemistry - A European Journal published by Wiley-VCH GmbH

metal) and the corresponding nanowires lead to a device with better saturation during irradiation, and moreover, complete relaxation thereafter.

Experimental Section

Sputter deposition

Zinc metal was deposited using a Cressington 208 HR at 60 mA and residual pressure of 0.05 mbar on quartz or TFT substrates (described in detail below in TFT measurement section). The thickness was monitored with a quartz microbalance (thickness controller MTM 20). Zinc sputter targets were obtained from Polymet with 99.99% purity. The conversion of the as-deposited films to zinc oxide was achieved by annealing the substrates on a hotplate.

Microwave reaction

Diaqua-bis[2-(methoxyimino) propanoato] zinc (**1**) was prepared according to the procedure published earlier.[67] For the nanowire deposition, aqueous solutions of (**1**) and HMTA were prepared separately and then mixed, so that 10 mM concentrations for both educts were obtained. Microwave reactions were performed in a Discover (CEM) microwave reactor with original CEM reaction tubes and silicon stoppers supplied by the manufacturer. Substrates were fixed at the side of the tubes with double-sided adhesive tape. The solution was heated to 70 °C and kept at this temperature for 10 min. The vessel was cooled to room temperature with compressive air. The substrates were removed carefully and cleaned by washing with a copious amount of distilled water, and were then dried in an argon stream.

TFT measurements

TFT substrates (1.5×1.5 cm^2, interdigital structure "Gen. 4", Fraunhofer IWS-Dresden, Germany) consisted of n-doped silicon with a 230 nm layer of SiO_2, on which gold electrodes were deposited with an intermediate adhesive layer of indium tin oxide (ITO). The channel width of source/drain electrodes was $W=10$ mm, with a channel length $L=10$ µm. TFT characteristics were determined with an HP 4155A Semiconductor Parameter Analyzer (Agilent) in a glovebox in the dark under controlled conditions (argon, H_2O exclusion). TFT devices were stored in darkness for about 24 h prior to measurement to exclude photoconductive effects. The charge carrier mobility μ_{SAT} and threshold voltage V_{th} were derived from a linear fitting of the square root of the source drain current ($I_{DS}{}^{0.5}$) as a function of gate source voltage V_{GS}.

UV photodetection measurements

Samples were irradiated with a Vilber Lourmat VL-6.LC (6 W, 365 nm). Switching was controlled using a timer clock for the supply voltage. Currents were measured with a Keithley 2700/7700/E digital multimeter. The data collection was automated and recorded using Labview software.

Characterization techniques

UV/Vis spectroscopy: Thermo Scientific Evolution 600. X-Ray diffraction (XRD): Miniflex 600 (Rigaku), CuK_α radiation, 600 W in Bragg–Brentano geometry. Scanning electron microscopy (SEM): Micrographs were obtained with an XL Series, Philips, XL30 FEG. Ellipsometry: Woollam M-2000 V spectrometer (spectral range 370–1690 cm^{-1}) using the CompleteEASE software (version 6.29). X-Ray photoelectron spectroscopy (XPS): Thermo Fisher Scientific, East Grinstead, UK. A monochromated $Al_{K\alpha}$ X-ray source with a spot size of 400 µm was used. The K alpha+ charge compensation system was used during the analysis, using electrons of 8 eV energy and low-energy argon ions to prevent any localized charge buildup. The spectra were fitted with one or more Voigt profiles (uncertainty: ±0.2 eV) and Scofield sensitivity factors were applied for quantification. All spectra were referenced to the C 1s peak of hydrocarbons at 285.0 eV by means of the well-known photoelectron peaks of metallic Cu, Ag, and Au, respectively.

Positron annihilation spectroscopy (PAS)

The positron lifetime investigations were performed at the Mono-energetic Positron Spectroscopy (MePS) beamline, which is the end station of the radiation source ELBE (Electron Linac for beams with high Brilliance and low Emittance) at HZDR, Germany.[68] A digital lifetime $CrBr_3$ scintillator detector with homemade software operating on SPDevices ADQ14DC-2X hardware with 14-bit vertical resolution, 2 GS s^{-1} horizontal resolution, and with a time-resolution function down to about 230 ps was utilized. All spectra contained at least 5×10^6 counts. The positron lifetime spectra represent a sum of time-dependent exponential decays $N(t)=\Sigma_i I_i/\tau_i\cdot\exp(-t/\tau_i)$ convoluted with Gaussian functions describing the spectrometer timing resolution. Spectra analysis was conducted using the nonlinearly least-squared-based package PALSfit fitting software.[69] An yttria-stabilized zirconia reference sample with well-defined single component positron lifetime, $\tau\approx181$ ps, was taken as a correction spectrum to account for undesirable background by means of subtracting not related to the sample positron lifetime components during the fitting procedure: ≈400–900 ps (<5%) and <55 ns (<1%) depending on positron implantation energy.

Acknowledgements

We acknowledge the technical support of E. Hirschmann (Helmholtz-Zentrum Dresden-Rossendorff e.V.). XPS measurements were performed at KNMF at KIT under contract 2019-023-027749. We thank V. Trouillet for this continuing collaboration. We acknowledge ellipsometric measurements by S. Heinschke (TUDa). Open access funding enabled and organized by Projekt DEAL.

Conflict of interest

The authors declare no conflict of interest.

Keywords: defect structures · nanostructures · positron annihilation · thin-film transistors · UV sensors · zinc oxide

[1] E. Espid, F. Taghipour, *Crit. Rev. Solid State* **2017**, *42*, 416–432.
[2] K. Kandpal, N. Gupta, *Microelectron. Int.* **2018**, *35*, 52–63.
[3] Z. X. Xu, Y. L. Zhang, Z. N. Wang, *J. Phys. D* **2019**, *52*, 223001.
[4] C. Brox-Nilsen, J. D. Jin, Y. Luo, P. Bao, A. M. Song, *IEEE Trans. Electron. Devices* **2013**, *60*, 3424–3429.
[5] C. W. Shih, A. Chin, *Sci. Rep.* **2017**, *7*, 1147.
[6] S. J. Kim, S. Yoon, H. Kim, *Jpn. J. Appl. Phys.* **2014**, *53*, 02BA02.
[7] C. Glynn, C. O'dwyer, *Adv. Mater. Interfaces* **2017**, *4*, 1600610.
[8] I. Bretos, R. Jiménez, J. Ricote, M. L. Calzada, *Chem. Soc. Rev.* **2018**, *47*, 291–308.

© 2020 The Authors. Chemistry - A European Journal published by Wiley-VCH GmbH

[9] A. Serrano, O. Caballero-Calero, M. A. Garcia, S. Lazic, N. Carmona, G. R. Castro, M. Martin-Gonzalez, J. F. Fernandez, *J. Eur. Ceram. Soc.* **2020**, *40*, 5535–5542.
[10] H. Beitollahi, S. Tajik, F. G. Nejad, M. Safaei, *J. Mater. Chem. B* **2020**, *8*, 5826–5844.
[11] M. D. McCluskey, *Semicond. Semimetals* **2015**, *91*, 279–313.
[12] L. Brillson, J. Cox, H. T. Gao, G. Foster, W. Ruane, A. Jarjour, M. Allen, D. Look, H. Von Wenckstern, M. Grundmann, *Materials* **2019**, *12*, 2242.
[13] K. Tang, S.-L. Gu, J.-D. Ye, S.-M. Zhu, R. Zhang, Y.-D. Zheng, *Chin. Phys. B* **2017**, *26*, 047702.
[14] K. Ellmer, A. Bikowski, *J. Phys. D* **2016**, *49*, 413002.
[15] K. Bandopadhyay, J. Mitra, *RSC Adv.* **2015**, *5*, 23540–23547.
[16] S. Pal, N. Gogurla, A. Das, S. S. Singha, P. Kumar, D. Kanjila, A. Singha, S. Chattopadhyay, D. Jana, A. Sarkar, *J. Phys. D* **2018**, *51*, 105107.
[17] D. Chen, F. Gao, M. D. Dong, B. Liu, *J. Mater. Res.* **2012**, *27*, 2241–2248.
[18] D. H. Kim, G. W. Lee, Y. C. Kim, *Solid State Commun.* **2012**, *152*, 1711–1714.
[19] I. Makkonen, E. Korhonen, V. Prozheeva, F. Tuomisto, *J. Phys. Condens. Matter* **2016**, *28*, 224002.
[20] S. K. Sharma, P. K. Pujari, K. Sudarshan, D. Dutta, M. Mahapatra, S. V. Godbole, O. D. Jayakumar, A. K. Tyagi, *Solid State Commun.* **2009**, *149*, 550–554.
[21] S. Hageraats, K. Keune, S. Stankic, S. Stanescu, M. Tromp, M. Thoury, *J. Phys. Chem. C* **2020**, *124*, 12596–12605.
[22] M. Zhang, F. Averseng, J. M. Krafft, P. Borghetti, G. Costentin, S. Stankic, *J. Phys. Chem. C* **2020**, *124*, 12696–12704.
[23] M. C. Biesinger, L. W. M. Lau, A. R. Gerson, R. S. C. Smart, *Appl. Surf. Sci.* **2010**, *257*, 887–898.
[24] J. C. Dupin, D. Gonbeau, P. Vinatier, A. Levasseur, *PhysChemComm* **2000**, *2*, 1319–1324.
[25] H. Z. Dong, J. C. Zhou, S. Virtanen, *Appl. Surf. Sci.* **2019**, *494*, 259–265.
[26] M. Fuentes, D. De La Fuente, B. Chico, I. Llorente, J. A. Jiménez, M. Morcillo, *Mater. Corros.* **2019**, *70*, 1005–1015.
[27] E. Diler, S. Rioual, B. Lescop, D. Thierry, B. Rouvellou, *Corros. Sci.* **2001**, *43*, 178–186.
[28] J. Duchoslav, M. Arndt, T. Keppert, G. Luckeneder, D. Stifter, *Anal. Bioanal. Chem.* **2013**, *405*, 7133–7144.
[29] J. I. Hong, J. Bae, Z. L. Wang, R. L. Snyder, *Nanotechnology* **2009**, *20*, 085609.
[30] J. Kennedy, P. P. Murmu, J. Leveneur, A. Markwitz, J. Futter, *Appl. Surf. Sci.* **2016**, *367*, 52–58.
[31] I. Bouanane, A. Kabir, D. Boulainine, S. Zerkout, G. Schmerber, B. Boudjema, *J. Electron. Mater.* **2016**, *45*, 3307–3313.
[32] M. Girtan, G. G. Rusu, S. Dabos-Seignon, M. Rusu, *Appl. Surf. Sci.* **2008**, *254*, 4179–4185.
[33] L. Li, W. Gao, R. J. Reeves, *Surf. Coat. Technol.* **2005**, *198*, 319–323.
[34] Y. G. Wang, S. P. Lau, H. W. Lee, S. F. Yu, B. K. Tay, X. H. Zhang, H. H. Hng, *J. Appl. Phys.* **2003**, *94*, 354–358.
[35] U. Diebold, L. V. Koplitz, O. Dulub, *Appl. Surf. Sci.* **2004**, *237*, 336–342.
[36] D. Mora-Fonz, T. Lazauskas, M. R. Farrow, C. R. A. Catlow, S. M. Woodley, A. A. Sokol, *Chem. Mater.* **2017**, *29*, 5306–5320.
[37] R. C. Hoffmann, J. J. Schneider, *J. Am. Ceram. Soc.* **2011**, *94*, 1878–1883.
[38] M. König, S. Höhn, R. Hoffmann, J. Suffner, S. Lauterbach, L. Weiler, O. Guillon, J. Rödel, *J. Mater. Res.* **2011**, *26*, 2125–2134.
[39] E. Suvaci, I. Ö. Özer, *J. Europ. Ceram. Soc.* **2005**, *25*, 1663–1673.
[40] D. Yoo, W. Jeon, J. Kim, J. Meng, Y. Yang, J. Jo, *J. Ceram. Soc. Japan* **2017**, *125*, 112–117.
[41] A. J. Flewitt, J. D. Dutson, P. Beecher, D. Paul, S. J. Wakeham, M. E. Vickers, C. Ducati, S. P. Speakman, W. I. Milne, M. J. Thwaites, *Semicond. Sci. Technol.* **2009**, *24*, 085002.
[42] B. Y. Oh, Y. H. Kim, H. J. Lee, B. Y. Kim, H. G. Park, J. W. Han, G. S. Heo, T. W. Kim, K. Y. Kim, D. S. Seo, *Semicond. Sci. Technol.* **2011**, *26*, 085007.
[43] M. O. Liedke, W. Anwand, R. Bali, S. Cornelius, M. Butterling, T. T. Trinh, A. Wagner, S. Salamon, D. Walecki, A. Smekhova, *J. Appl. Phys.* **2015**, *117*, 163908.
[44] Z. Wang, C. Luo, W. Anwand, A. Wagner, M. Butterling, M. A. Rahman, M. R. Phillips, C. Ton-That, M. Younas, S. Su, *Sci. Rep.* **2019**, *9*, 3534.
[45] D. J. Winarski, W. Anwand, A. Wagner, P. Saadatkia, F. A. Selim, M. Allen, B. Wenner, K. Leedy, J. Allen, S. Tetlak, D. C. Look, *AIP Adv.* **2016**, *6*, 095004.
[46] K. M. Johansen, F. Tuomisto, I. Makkonen, L. Vines, *Mater. Sci. Semicond. Process.* **2017**, *69*, 23–27.
[47] C. Bazioti, A. Azarov, K. M. Johansen, B. G. Svensson, L. Vines, A. Y. Kuznetsov, Ø. Prytz, *J. Phys. Chem. Lett.* **2019**, *10*, 4725–4730.
[48] J. J. Jia, A. Suko, Y. Shigesato, T. Okajima, K. Inoue, H. Hosomi, *Phys. Rev. Appl.* **2018**, *9*, 014018.
[49] F. Tuomisto, I. Makkonen, *Rev. Mod. Phys.* **2013**, *85*, 1583–1631.
[50] R. C. Hoffmann, N. Koslowski, S. Sanctis, M. O. Liedke, A. Wagner, M. Butterling, J. J. Schneider, *J. Mater. Chem. C* **2018**, *6*, 9501–9509.
[51] G. Syrrokostas, K. Govatsi, S. N. Yannopoulos, *Cryst. Growth Des.* **2016**, *16*, 2140–2150.
[52] M. Skompska, K. Zarębska, *Electrochim. Acta* **2014**, *127*, 467–488.
[53] R. Ahson, R. Ahmad, F. E. Mubarik, A. J. Flewitt, *J. Nanoelectron. Optoelectron.* **2019**, *14*, 1451–1460.
[54] D. Sakai, K. Nagashima, H. Yoshida, M. Kanai, Y. He, G. Z. Zhang, X. X. Zhao, T. Takahashi, T. Yasui, T. Hosomi, *Sci. Rep.* **2019**, *9*, 14160.
[55] A. Pimentel, A. Samouco, D. Nunes, A. Araujo, R. Martins, E. Fortunato, *Materials* **2017**, *10*, 1308.
[56] A. S. Rana, M. Kang, H. S. Kim, *Sci. Rep.* **2016**, *6*, 24870.
[57] S. Sanctis, R. C. Hoffmann, S. Eiben, J. J. Schneider, *Beilstein J. Nanotechnol.* **2015**, *6*, 785–791.
[58] T. T. Yin, N. Chen, Y. Y. Zhang, X. Y. Cai, Y. D. Wang, *Superlattices Microstruct.* **2014**, *74*, 279–293.
[59] T. Cossuet, H. Roussel, J. M. Chauveau, O. Chaix-Pluchery, J. L. Thomassin, E. Appert, V. Consonni, *Nanotechnology* **2018**, *29*, 475601.
[60] A. U. Pawar, C. W. Kim, M. J. Kang, Y. S. Kang, *Nano Energy* **2016**, *20*, 156–167.
[61] M. R. Alenezi, T. H. Alzanki, A. M. Almeshal, A. S. Alshammari, M. J. Beliatis, S. J. Henley, S. R. P. Silva, *RSC Adv.* **2015**, *5*, 103195–103202.
[62] M. R. Alenezi, S. J. Henley, S. R. P. Silva, *Sci. Rep.* **2015**, *5*, 8516.
[63] K. L. Foo, M. Kashif, U. Hashim, M. E. Ali, *Optik* **2013**, *124*, 5373–5536.
[64] F. Yi, Q. L. Liao, X. Q. Yan, Z. M. Bai, Z. Z. Wang, X. Chen, Q. Zhang, Y. H. Huang, Y. Zhang, *Physica E* **2014**, *61*, 180–184.
[65] F. V. E. Hensling, D. J. Keeble, J. Zhu, S. Brose, C. Xu, F. Gunkel, S. Danylyuk, S. S. Nonnenmann, W. Egger, R. Dittmann, *Sci. Rep.* **2018**, *8*, 8846.
[66] H. Seo, Y. J. Cho, J. Kim, S. M. Bobade, K. Y. Park, J. Lee, D. K. Choi, *Appl. Phys. Lett.* **2010**, *96*, 222101.
[67] J. J. Schneider, R. C. Hoffmann, J. Engstler, S. Dilfer, A. Klyszcz, E. Erdem, P. Jakes, R. A. Eichel, *J. Mater. Chem.* **2009**, *19*, 1449–1457.
[68] A. Wagner, W. Anwand, A. G. Attallah, G. Dornberg, M. Elsayed, D. Enke, A. E. M. Hussein, R. Krause-Rehberg, M. O. Liedke, K. Potzger, T. T. Trinh, *J. Phys. Conf. Ser.* **2017**, *791*, 012004.
[69] J. V. Olsen, P. Kirkegaard, N. J. Pedersen, M. Eldrup, *Phys. Status Solidi C* **2007**, *4*, 4004–4006.

Manuscript received: September 21, 2020
Accepted manuscript online: November 26, 2020
Version of record online: ■■ ■■, 0000

© 2020 The Authors. Chemistry - A European Journal published by Wiley-VCH GmbH

doi.org/10.1002/chem.202004270

FULL PAPER

Thin-film transistors: Zinc oxide layers can be obtained conveniently through the oxidation of sputter-deposited thin films of zinc metal at temperatures between 250 and 450 °C. Positron annihilation studies hint at vacancy clusters rather than isolated point defects as the dominating feature in the defect chemistry of these films. This allows the description of the influence of annealing temperature on the resulting electronic performance of the semiconducting layers in thin-film transistors.

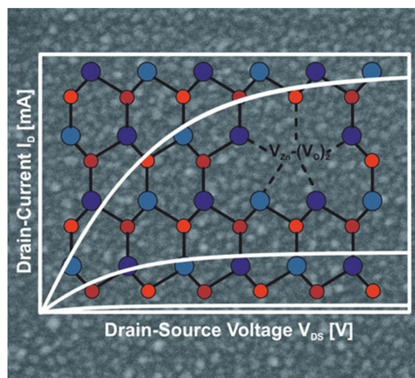

Positron Annihilation

*R. C. Hoffmann, S. Sanctis, M. O. Liedke, M. Butterling, A. Wagner, C. Njel, J. J. Schneider**

■■–■■

Zinc Oxide Defect Microstructure and Surface Chemistry Derived from Oxidation of Metallic Zinc: Thin-Film Transistor and Sensor Behavior of ZnO Films and Rods

© 2020 The Authors. Chemistry - A European Journal published by Wiley-VCH GmbH